17th AIAA/CEAS Aeroacoustics Conference (32nd AIAA Aeroacoustics Conference)
05 - 08 June 2011, Portland, Oregon

AIAA 2011-2875

Effect of CFD Wake Prediction in a Hybrid Simulation of Fan Broadband Interaction Noise

Sheryl M. Grace * and Jeremy Maunus † and Douglas L. Sondak ‡
Boston University, Boston, MA 02215

A fully computational hybrid method for simulating broadband interaction noise downstream of the fan stage in a turbofan engine is explored in this paper. The particular noise source of interest is due to the interaction of the fan rotor wake with the fan exit guide vanes (FEGVs). The broadband noise is predicted with the RSI code coupled to a Reynolds Averaged Navier Stokes (RANS) flow simulation. Input flow quantities for the RSI calculation of the FEGV response are derived from the rotor wake flow predicted by four different RANS simulations. The RANS solutions are shown to be in reasonable agreement with each other and with the hot-wire data available at the approach condition. The RANS solutions differ from each other more at higher rotor speeds but are self consistent in their wake flow predictions across the 3 rotor speeds: approach, cutback, and takeoff. RANS solutions from different codes run by different users will never be in exact agreement and as such will lead to differing input quantities for RSI. A sensitivity study is presented to highlight the effect of differences in the input quantities on the broadband noise predictions from RSI. It is shown that differences in the background turbulence intensity level and the average turbulence length scale have the largest impact on the prediction. The general findings are used to interpret the differences in the predictions obtained with RSI when the input is based on the RANS simulations. While the need for accurate background turbulence intensity and turbulent length scale prohibit a quantitatively accurate broadband noise prediction with present RANS approaches, it is shown that the trend in the downstream broadband noise from rotor-FEGV interaction with rotor speed can be predicted correctly. This accurate trend prediction requires that the stagger angle in the RSI model be matched to the trailing edge stagger and that the input quantities be based on a self-consistent set of RANS simulations across the rotor speeds.

Nomenclature

B	number of rotor blades
c_o	mean speed of sound in bypass duct
h	rotor spacing
i	$\sqrt{-1}$
J_m, Y_m	Bessel functions order m
$\mathbf{k}, \mathbf{k}$	wave number vectors associated with $\mathbf{X}$ and $\mathbf{Y}$
M	Mach number in bypass duct
r	radial coordinate
t, τ	time
$\mathbf{u}_1$	perturbation state vector
$\mathbf{u}'_\mathbf{b}$	value of background turbulence intensity at given radial location
$\mathbf{u}'_\mathbf{w}$	value of centerline turbulence intensity (without the background) at given radial location
U_r	mean flow speed in vane frame (assumed alligned with chord direction)

*Assoc. Prof., Dept. Mech. Eng., Associate Fellow, AIAA. sgrace@bu.edu.
†Graduate student, Dept. of Mech. Eng., student member AIAA.
‡Scientific Computing and Visualization, Member AIAA.

V	number of vanes
$\mathbf{W}$	mean streamwise velocity in rotor frame
W_h	width of turbulence intensity Gaussian fit at half centerline intensity
$\mathbf{v}'$	perturbation velocity vector
$\mathbf{x}$	vane frame coordinate vector
$\mathbf{X}, \mathbf{Y}$	rotor frame coordinate vector s
β	$\sqrt{1-M^2}$
χ	stagger angle
ϵ	dissipation rate
Λ	integral length scale
ω, ν	radial frequencies related to t and τ
Ω	fan rotation rate
ρ_o	mean density
CFD	Computational Fluid Dyanmics
FEGV	Fan Exit Guide Vane
HW2	Hot wire data at the location near the leading edge of the vane
NC	Number of chordwise points
RANS	Reynods Averaged Navier Stokes
RSI	Rotor-Stator Interaction code distributed by NASA
SDT	source diagnostic test
TKE	Turbulent Kinetic Energy

I. Introduction

The interaction between turbulence in a fan rotor wake and the fan exit guide vanes (FEGVs) contributes to the broadband noise associated with the fan-stage of a turbofan engine. Methods for predicting the broadband noise due to the interaction of the wakes and the FEGVs have been presented in the literature.[1–4] These prediction methods use a two step process in which the turbulence in the rotor wake flow is characterized and then the response of the FEGV to the turbulence is computed. In all of the methods, the vane response computation is based on the solution to the linearized Euler equations for a simplified geometry. Some of the methods use 2D strip theory with flat-pate vanes[1,2] and another uses a 3D flat cambered representation of the vanes.[4] Some of the methods compute the associated response via analytical Green's function methods for acoustic propagation in a duct and some assume cascade like propagation away from the vane.

In all cases, the input is derived from the turbulence characteristics in the wake. The methods differ in how the wake information is utilized. For instance, some require knowledge of the passage distribution of turbulence intensity while others only utilize the average passage value of turbulent kinetic energy (TKE). In the past, experimental data have been used to specify the FEGV inflow. More recently, researchers have attempted to develop a fully computational method for the broadband noise prediction. For instance, the fully computational method described in[2,3] relies on RANS CFD to provide turbulent parameters in the wake and computes the broadband vane response via the RSI method.

The present research investigates further the fully computational hybrid scheme by studying the effect that variation in the prediction of the wake turbulence has on the simulation of the broadband noise by the RSI method.

A brief review of the RSI methodology is given in the next section. The effect of basic input parameter modifications on the predicted broadband noise is shown in Section III. Section IV provides analysis of the turbulent wake characteristics for the SDT and describes the method utilized to obtain the relevant input wake parameters from RANS. Finally, a comparison between predictions of the broadband noise based on four different RANS results is given.

II. Method

The aerodynamic core that forms the basis of the RSI code was originally developed by Ventres.[5] Figure 1 gives a schematic of the fan rotor and the simplified FEGV geometry used in RSI. It utilizes a a two-dimensional semianalytical solution for the response of a flat-plate cascade[5] to a 2D gust. Strip theory is then used to account for the three-dimensional effects. The resulting vane pressure distribution at a given frequency and wave number is coupled to the acoustics downstream of the vane via the Green's function for a cylindrical annulus.

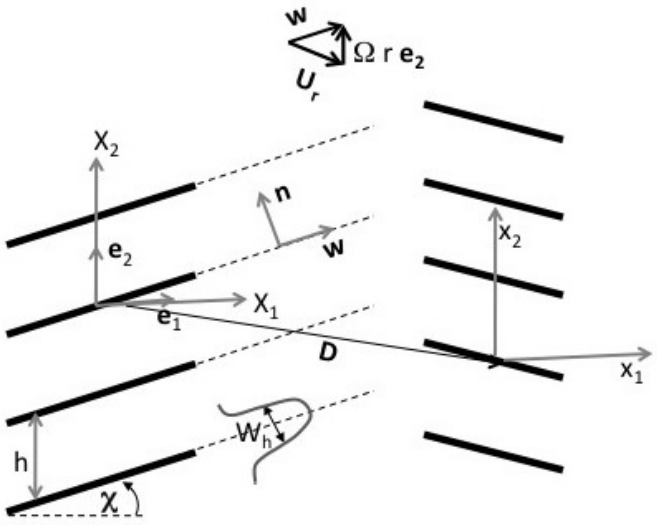

Figure 1. 2D flat plate cascade nomenclature.

In this study the sound power spectrum at the exit of the fan duct is of interest. The overall method to compute the sound power spectrum is developed based on the physics which dictates that 1) the sound power spectrum is obtained from the pressure spectrum on an axial plane downstream of the FEGV; 2) the pressure spectrum at any point in the duct is related through the Green's function to the unsteady vane pressure spectrum; and 3) the unsteady vane pressure spectrum is produced by the inflow wake turbulence. A progression backwards through the physical connections shows how RSI models the broadband response.

The turbulent fluctuations can be described in the rotating frame of reference as

$$w(r, \mathbf{X}, t) = u_c' F(\mathbf{X} \cdot \mathbf{n}) g(r, \mathbf{X} - \mathbf{W}t) \qquad (1)$$

with $\mathbf{W}$ describing the mean flow velocity and u_c' representing the streamwise rms turbulence intensity on the wake centerline. (Note the assumption of isotropy has been applied here.) g is a stationary random function. F is a periodic function in the direction normal to wake centerline. If B fan rotor blades have spacing $h = 2\pi r/B$ and stagger χ at a given radial location, a representative distribution f of the turbulence intensity in a passage can be repeated behind each rotor so a general form of F is given as

$$F(\mathbf{X} \cdot \mathbf{n}) = \sum_m f(\mathbf{X} \cdot \mathbf{n} - mh\cos\chi) \qquad (2)$$

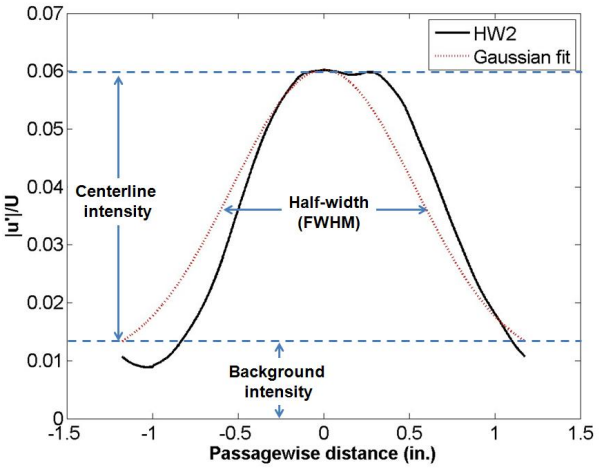

Figure 2. Gaussian representation of turbulence intensity.

Poisson's formula then states that

$$F(\mathbf{X} \cdot \mathbf{n}) = \frac{1}{h\cos\chi} \sum_s \hat{f}\left(\frac{s}{h\cos\chi}\right) \exp\left(i2\pi \frac{s}{h\cos\chi} \mathbf{X} \cdot \mathbf{n}\right) \qquad (3)$$

where $\hat{f}$ is the Fourier transform of f. In practice F is interpreted as being a combination of a background value and Eq. (3) with f modelled as a Guassian function as shown in Figure 2. Therefore

$$f(\mathbf{X} \cdot \mathbf{n}) = \exp\left(-\pi (\mathbf{X} \cdot \mathbf{n})^2 / W_h^2\right) \qquad (4)$$

where W_h is the width of the Gaussian distribution at half the centerline height and $u'_c F$ becomes

$$u'F = u'_b + u'_w \frac{W'_h B}{2\pi r} \sum_s \exp\left[-\left(\frac{sBW'_h}{r} \right)^2 /(4\pi) \right] \exp\left[isBX_2/r \right] \tag{5}$$

where u'_b represents the background level of the turbulence intensity and u'_w is taken as the centerline value of a Gaussian fit to the turbulence intensity above the background.

The end prediction relies on the turbulence spectrum such that it is necessary to consider the correlation of the turbulent velocity:

$$< w(r_1, \mathbf{X} - \mathbf{W}t) w(r_2, \mathbf{Y} - \mathbf{W}t) >= u'^2 F(\mathbf{X} \cdot \mathbf{n}) F(\mathbf{Y} \cdot \mathbf{n}) \phi_W[\mathbf{X} - \mathbf{Y} - \mathbf{W}(t - \tau), \Delta r] \tag{6}$$

Δr is the average radial location and it is assumed that $r_1 = r_2 = r$ except in Δr. ϕ_W is also periodic and it is assumed that this autocorrelation function can be represented as

$$\phi_W(\mathbf{X}, \Delta r) = \phi_1 \left(\frac{X_1}{\Lambda_1} \right) \phi_2 \left(\frac{X_2}{\Lambda_2} \right) \phi_r \left(\frac{X_r}{\Lambda_r} \right) \tag{7}$$

where $\Lambda_1, \Lambda_2, \Lambda_r$ are integral length scales. A further assumption is made in RSI that the statistics represented by ϕ_1, ϕ_2, and ϕ_r are Gaussian.

Therefore, if one takes the normalized unsteady pressure response to a unit upwash disturbance in the frequency domain at a particular radial vane section to be denoted p_{non}, the actual expected value of the unsteady pressure response is given by

$$\begin{aligned} < \Delta\overline{p}_{s_1}(r, z, \omega) \Delta\overline{p}_{s_2}(r' z' \nu) >= \frac{(\rho_o U_r)^2}{(2\pi)^4} \int\int p_{non}(r, z, \mathbf{k}, \omega) \exp[i s_1 \mathbf{k} \cdot \mathbf{h}] \\ \int\int p^*_{non}(r', z', \mathbf{K}, \nu) \exp[-i s_2 \mathbf{K} \cdot \mathbf{h}] \\ < \hat{\hat{\overline{w}}}(r, \mathbf{k}, \omega) \hat{\hat{\overline{w}}}^*(r', \mathbf{K}, \nu) > d^2\mathbf{k}\ d^2\mathbf{K} \end{aligned} \tag{8}$$

p_{non} here is obtained from the integral solution for a 2D cascade response to a gust and s_1 and s_2 reference individual vanes. The expected value of the unsteady pressure at a point in the duct is then given by

$$\begin{aligned} < \overline{p}_{mn}(\omega) \overline{p}^*_{mn}(\nu) >= \frac{1}{4\Gamma^2 k_{mn}(\omega) k_{mn}(\nu)} \int_{r_H}^{r_D} \psi_m(k_{mn}(\omega) r)[(m/r)\cos\theta' - \gamma_{mn}(\omega)\sin\theta'] \\ \int_{r_H}^{r_D} \psi_m(k_{mn}(\nu) r')[(m/r')\cos\theta' - \gamma_{mn}(\nu)\sin\theta'] \\ \int_{-b}^{b} \exp\left[i\mu(r, \omega) z \right] \int_{-b'}^{b'} \exp\left[-i\mu(r'\nu) z' \right] \\ \sum_{s_1=0}^{V-1} \exp\left[i 2\pi m s_1 / V \right] \sum_{s_2=0}^{V-1} \exp\left[-2\pi m s_2 / V \right] < \Delta\overline{p}_{s_1}(r, z, \omega) \Delta\overline{p}^*_{s_2}(r' z' \nu) > dz\ dz'\ dr\ dr' \end{aligned} \tag{9}$$

with

$$\mu(r, \omega) = \gamma_{mn}(\omega)\cos\theta' + (m/r)\sin\theta' \tag{10}$$

$$\psi_m(\kappa_{mn} r) = A J_m(\kappa_{mn} r) + B Y_m(\kappa_{mn} r) \tag{11}$$

$$\kappa_{mn} \quad \text{are the eigenfrequencies of the radial equation} \tag{12}$$

$$A = 1 \tag{13}$$

$$B = -\frac{A J'_m(\kappa_{mn} r_D)}{Y'_m(\kappa_{mn} r_D)} \tag{14}$$

$$\gamma_{mn} = \frac{1}{\beta^2} \left(\frac{M\omega}{c_o} \pm k_{mn} \right) \tag{15}$$

$$k_{mn} = \sqrt{ \left(\frac{\omega}{c_o} \right)^2 - \beta^2 \kappa^2_{mn} } \tag{16}$$

$$\Gamma = \pi(r_D^2 - r_H^2) \tag{17}$$

The expected value of the power at an axial location along the duct is

$$< \overline{Power} >= \int \frac{\Gamma}{\rho_o U_r} \sum_m \sum_n \frac{M^2 \beta^4 (\omega/U_r) k_{mn}(\omega)}{[\omega/c_o - M k_{mn}(\omega)]^2} < \overline{p}_{mn} \overline{p}^*_{mn} > \frac{d\omega}{2\pi} \tag{18}$$

One can find the Fourier transform of Eq. (6) and carry out the successive integrations. The final form of the expected value of the duct pressure is given in both the Ventres report[5] and the Nallasamy and Envia paper.[2] Because the transforms are computed explicitly over k_1 and k_2 and the autocorrelation is allowed to differ in the three spatial directions, the RSI method is fundamentally different than methods in which the vane response is weighted by a three dimensional turbulence spectrum description. Also, the RSI method incorporates the distribution of the turbulence intensity within a passage whereas the other methods assume a single passage averaged value for the turbulence intensity. It is further noted that the selection of a Gaussian distribution for the turbulence intensity in a rotor passage and the selection of Gaussian statistics for the autocorrelation functions does not translate to the usage of a 3D Gaussian spectrum for the upwash spectrum (as might be chosen for use in other broadband methods).

In practice, to run RSI a user must specify several geometry and nondimensional flow quantities at each radial strip from hub-to-tip including: the chordlength; the stagger angle; the mean flow (axial and tangential Mach numbers); the background turbulence level in the passage u'_b; the centerline turbulence intensity in the passage u'_w; the width of the turbulence intensity profile at half max intensity W_h; and the three length scales Λ_1, Λ_2, and Λ_3. The next section demonstrates how some of these parameters impact the final prediction of broadband noise. The turbulent velocities are normaizled by the mean absolute velocity and the lengths are normalized by the vane outer radius.

III. Parameter study

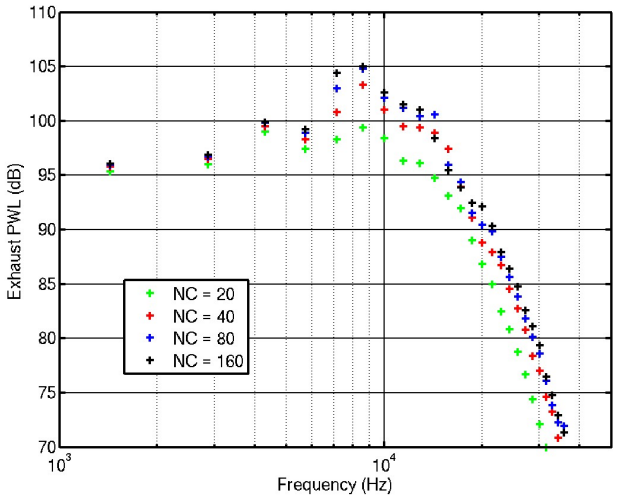

Figure 3. Effect of chordwise number of points on broadband computation.

For the general parameter study, nominal input values for the geometry and flow parameters related to the source diagnostic test (SDT) were derived. The nondimensional unsteady response of the vane to a unit disturbance p_{non} is calculated using the integral formulation and is dependent upon the number of collocation points (NC) used in the integration. As such, a grid convergence test was completed. The results shown in Figure 3 correspond to the downstream interaction noise spectrum. As expected, at lower frequencies (< 7000) little is gained from higher resolution. At higher frequencies little difference is seen in the prediction based on 80 or 160 chordwise points. As such, to save on computing time an NC of 80 was used for all subsequent calculations.

The FEGVs in RSI are modeled as flat plates. Therefore the user must select a stagger angle for the vanes. Figure 4(a) shows the radial distributions of the FEGV stagger angle computed three ways. The blue line was determined using a 90%/10% weighted average of the leading edge and trailing edge stagger angles respectively, while the cyan line was determined using a 50%/50% weighted average. The red line was determined using a 10%/90% weighted average. Figure 4(b)-(d) shows that for frequencies below roughly 10,000 Hz, an increase in stagger angle results in an increase in predicted exhaust PWL. At frequencies above 10,000 Hz, however, an increase in the stagger angle results in a steeper slope of the acoustic power spectrum.

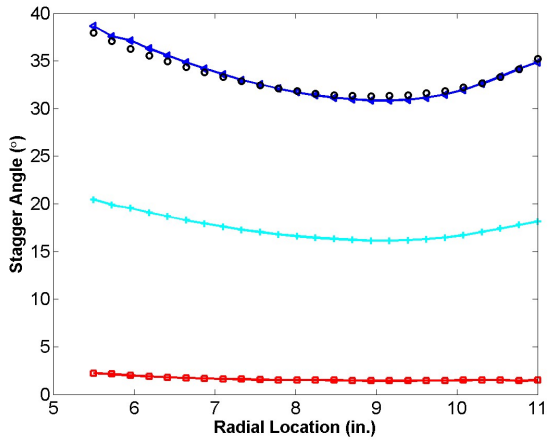

(a) Radial distribution of stagger angle

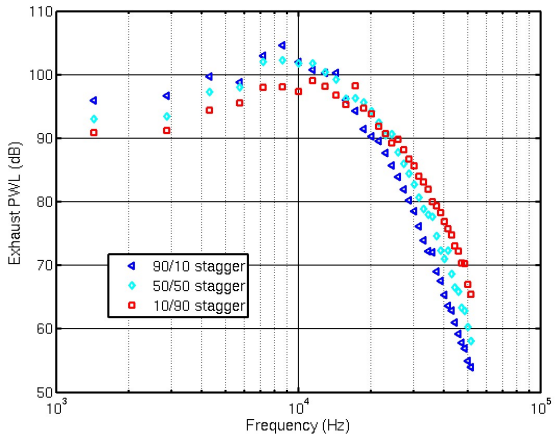

(b) Approach case

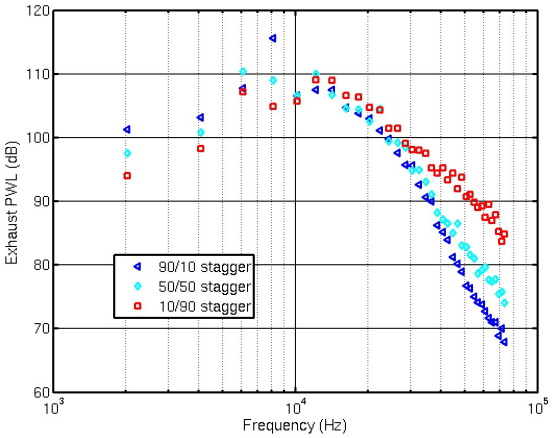

(c) Cutback case

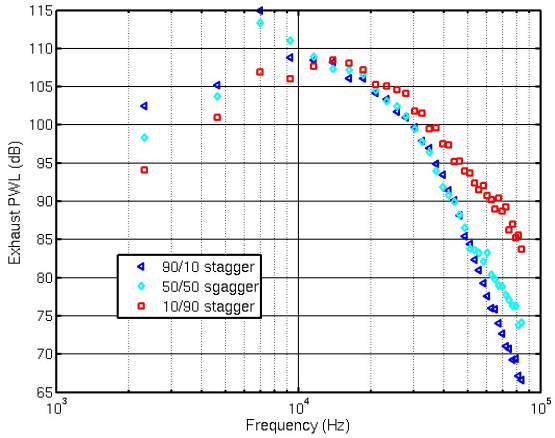

(d) Takeoff case

Figure 4. Effect of stagger angle on Exhaust PWL Spectrum

The effect of the turbulence input parameters was also considered. First, the value of the background turbulence intensity was changed. The results when the background is neglected (set to zero) or doubled at all radial locations are shown in Figure 5. Similarly, the sensitivity to general changes in the the centerline intensity and the full-width at half maximum (FWHM) intensity is shown in Figure 5. All else being equal, on average across the frequencies considered here, doubling or zeroing out the background intensity has a larger effect on the predicted exhaust PWL than making the same modification to the centerline intensity. Moreover, on average across the entire frequency range, changes in the FWHM had the least impact on the PWL. The sensitivity to these turbulence parameters can be understood in terms of the average value of the turbulence intensity across the passage. It is clear from Figure 2 that the average passage value of the turbulence intesity is more affected by a doubling of the background value than either doubling the height or width of the Gaussian.

The influence of length scale was also investigated. Three values must be specified that correspond to the length scales associated with the longitudinal (Λ_1) and two transverse directions (Λ_2, Λ_3). For isotropic flow the length scale ratio is nearly 2:1:1. The sensitivity to adjustments of this ratio is shown in Figure 5(d). As found previously by Atassi and Logue with their broadband code BB3D,[4] an increase in the longitudinal integral scale gives an increase in the predicted exhaust PWL at lower frequencies while at higher frequencies it leads to a steeper drop off in the exhaust power spectrum. The ratio 2:1:2 has also been considered because it was used previously by Nallasamy.[2] The difference between the noise prediction with 2:1:1 and 2:1:2 is minimal with 2:1:2 leading to a roughly 2dB higher prediction across all frequencies.

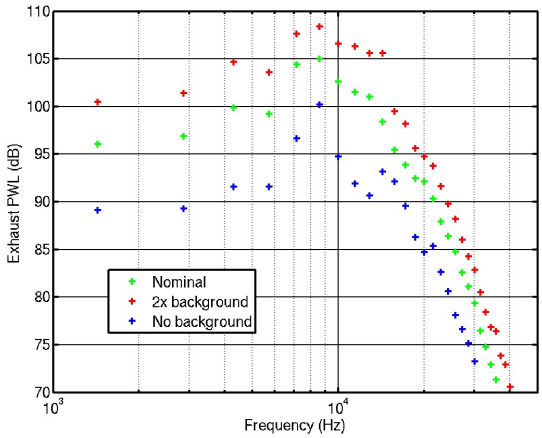

(a) Background intensity

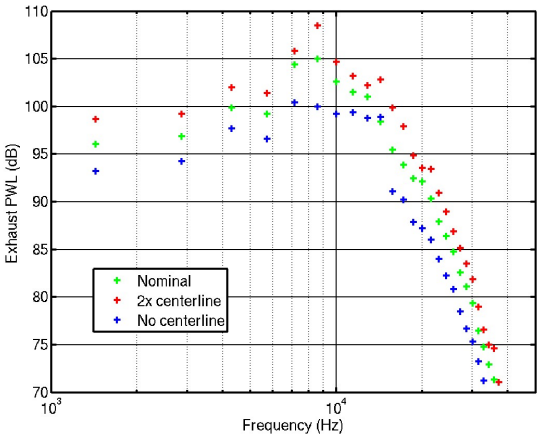

(b) Centerline intensity

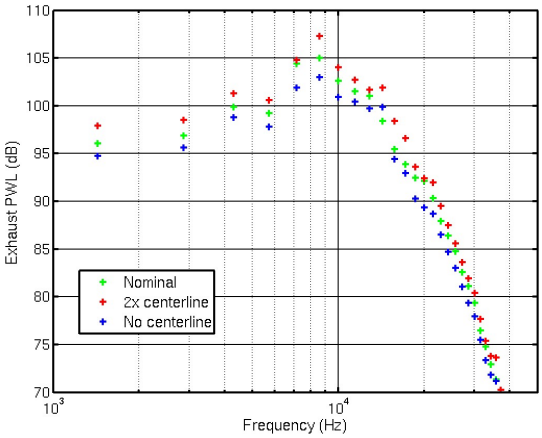

(c) FWHM

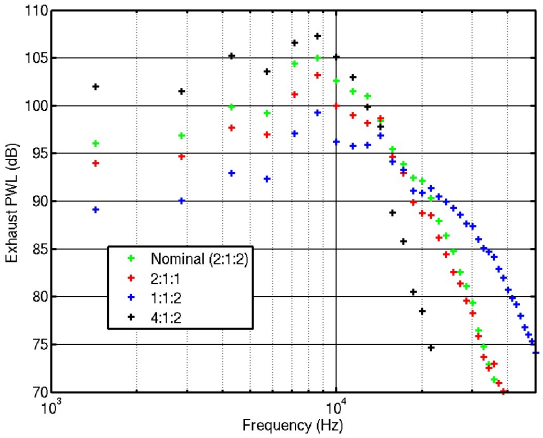

(d) Lengthscale

Figure 5. Effect of turbulence inputs on Exhaust PWL Spectrum at approach.

This general parametric behavior is used to illuminate the influence of CFD based input parameters on the broadband noise prediction in a fully coupled computational hybrid scheme.

IV. Validation of CFD output and comparison of RSI input

A critical component of the computational hybrid method is the prediction of the wake flow via CFD and the translation of the CFD quantities into useful input for the RSI calculation. RANS CFD that utilizes two-equation turbulence models provides values of the turbulent kinetic energy and a second quantity related to the dissipation. From this information, the model of the passagewise distribution of turbulence intensity, u'_b, u'_w, W_h and the length scales required for ϕ_W must be obtained. It is of interest then to benchmark the turbulence parameters provided by a given RANS CFD.

The benchmark for this study is the source diagnostic test (SDT) scaled turbofan experiment.[2,6] The SDT consisted of a fan stage with a 22" rotor and 3 vane configurations. This study utilizes the baseline vane geometry of 54 vanes. Several wheel speeds were tested experimentally three of which have been extensively discussed in the literature: the approach, the cutback, and the takeoff speeds.

As part of SDT, hot-wire measurements were acquired in the gap between the rotor and the FEGV for the lower wheel speed case. The hot-wire velocity measurements taken behind a rotor have strong periodic unsteadiness related to the blade passing frequency and its harmonics. Consequently, this deterministic unsteadiness must be removed from the signal to capture the truly turbulent velocity fluctuations. As such,

the velocity vector at a given location in such a system can be decomposed into a turbulent component and a time-dependent mean:

$$\mathbf{u}(t) = \mathbf{U}(\mathbf{x}, t) + \mathbf{u}'(\mathbf{x}, t) \tag{19}$$

The average-passage velocity is computed by time-averaging the measurements at each radial location for each circumferential location across a fan blade passage. The turbulent fluctuations are then calculated by subtracting the average-passage velocity (as a function of radial and circumferential position) from the instantaneous velocity. Turbulence intensity follows directly. The dissipation rate at a point in the flow can be determined from the experimental data by utilizing structure functions. The method is described in detail in Appendix A. The integral turbulent length scales can be computed from the hot-wire data at each radial location by way of integration of the autocorrelation:[7,8]

$$\Lambda_i = \frac{\overline{U_1}}{\overline{u_i'^2}} \int_0^\infty u_i'(\tau) u_i'(\tau + t) dt. \tag{20}$$

where u_i is the entire time signal of the turbulent fluctuations at a given radial position. This method only provides the passage averaged length scale and cannot be used to obtain the distribution within a passage. More detail concerning the analysis of the hot-wire data is given in the work of Maunus.[9,10]

Flow solutions for the SDT baseline geometry from four proprietary RANS based CFD simulations were obtained. Some details regarding the codes and their prediction of basic flow quantities are reported in Appendix B.

The turbulent kinetic energy and mean dissipation across a passage at midspan as determined from the experimental data and the 4 CFD solutions are compared in Figures 6 and 7. In addition, Figure 6 and 7 show the comparison of the average passage values from hub to tip. The radial trends of the passage averaged values are captured relatively well by each of the RANS simulations. The magnitude of ϵ differs greatly between the experimental and computed values. The passagewise distributions of both the TKE and ϵ show less agreement and suggest that some of the simulations were run using limiters to fix the low end value of these parameters.

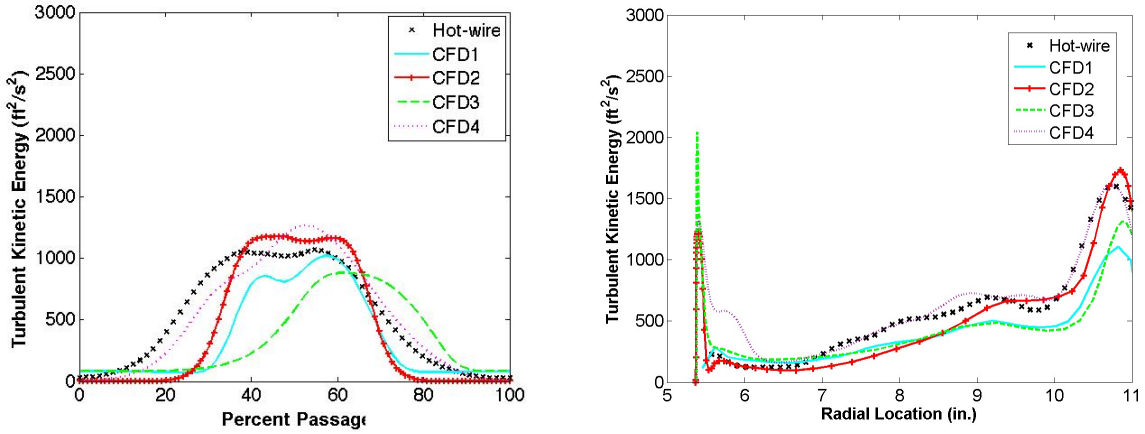

(a) HW2: Passage distribution.

(b) HW2: Circumferentially averaged.

Figure 6. Turbulenct Kinetic Energy

A length scale can be deduced from the RANS turbulence parameters via

$$\Lambda = C_\epsilon \frac{TKE^{\frac{3}{2}}}{\epsilon} \tag{21}$$

as shown in Appendix C. The method described in the Appendix leads to the selection of C_ϵ on the order of 0.02. However, traditionally in CFD, C_ϵ is selected to be 1.0. That the turbulence models have been developed such that the length scale is nominally recovered with $C_\epsilon = 1.0$ indicates that the value of ϵ computed via the RANS will not share the magnitude of ϵ computed from the experimental data using the

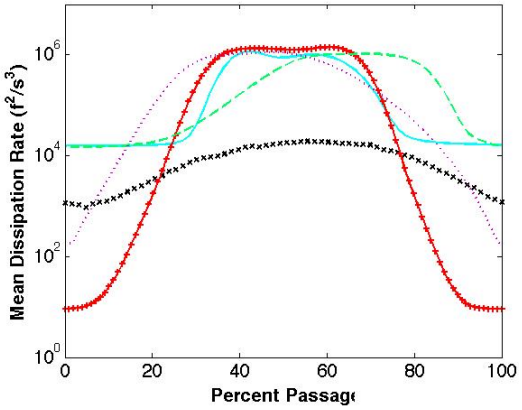

(a) HW2: Passage distribution.

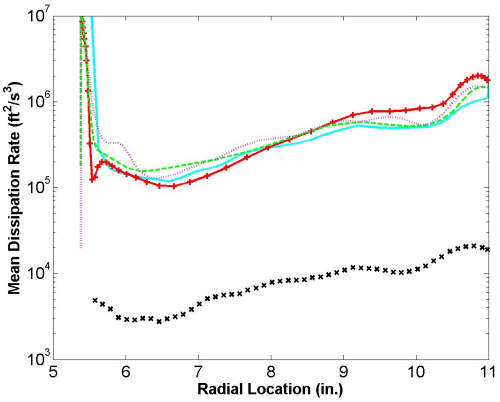

(b) HW1: Circumferentially averaged.

Figure 7. Mean dissipation

structure functions. This is obvious in Figures 7 and 8. The C_ϵ used with the experimental data was 0.02 which means that the ϵ from the experiment should be about 50 times smaller than that from the CFD and indeed this is the case. The agreement between the RANS based length scale and the experimental streamwise (or longitudinal) integral length scale is reasonable for all but the rotor alone RANS simulation CFD4

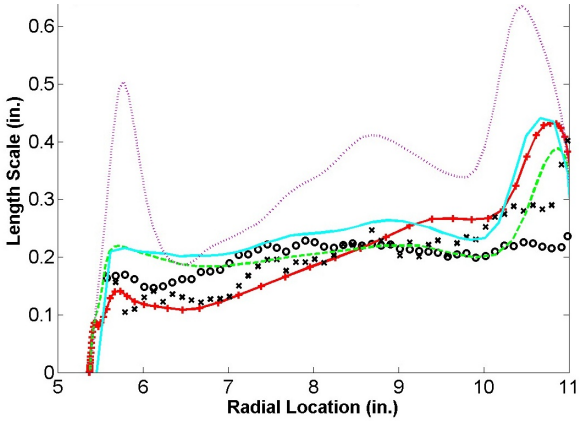

Figure 8. Integral Length Scale

RSI input data were derived from the RANS solutions and the experimental results (when available). First, the average passage mean flow at each radial location was determined. The comparison of this parameter with experimental data for the approach case is shown in Figure 9. The axial and tangential Mach numbers agree well for the approach case. For the takeoff case, the experimental values of the mean flow are not shown and it can be seen that there is a larger spread amongst the CFD predictions here.

When isotropic turbulence is assumed, the turbulence intensity is related to the turbulent kinetic energy via $u'_{RANS} = \sqrt{\frac{2}{3} TKE_{RANS}}$. The passagewise distributions of the turbulence intensity shown in Figure 6 are fitted with background and Gaussian parameters at each radial location. Refer to Figure 2 for this fitting.

The various predictions of the background, centerline, and wake width values as a function of radial position are shown in Figure 10 for both approach and takeoff conditions. Of note is the difference in the background turbulence level. For the approach case, two simulations have almost no background level and two have about double the level of the experiment. The trend in the CFD based values is the same for the takeoff case. The radial distribution of length scale for the approach speed were already shown in Figure

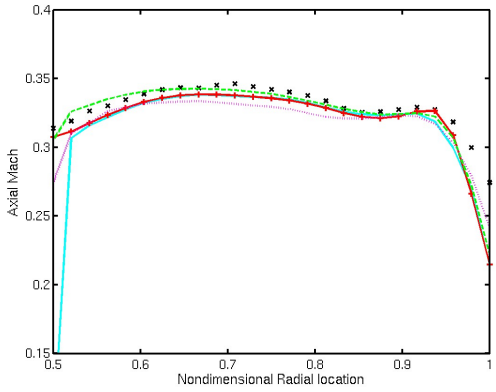

(a) Axial Mach number. Approach case.

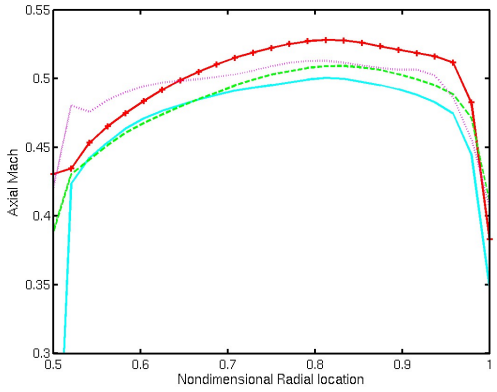

(b) Axial Mach number. Takeoff case.

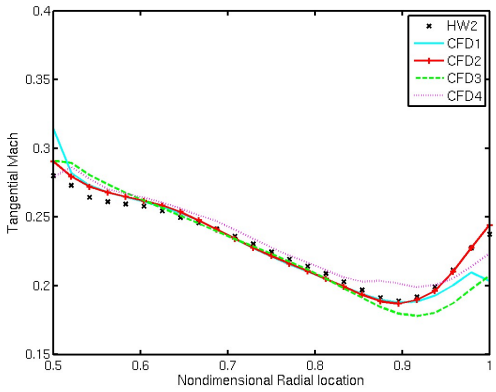

(c) Tangential Mach number. Approach case.

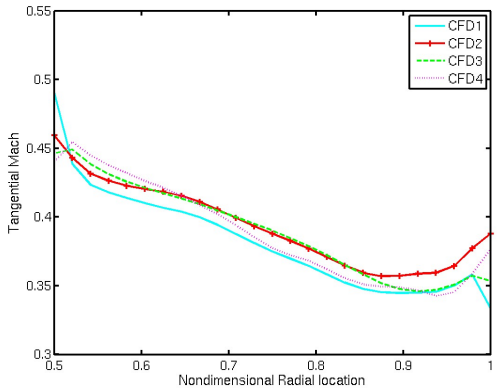

(d) Tangential Mach number. Takeoff case.

Figure 9. RSI mean inflow parameter comparison.

8. Figure 12 shows the length scales computed from the CFD for the takeoff case. From low to high wheel speeds, the codes give comparable results. For instance, CFD2 has the lowest turbulence intensity for all speeds, and CFD4 has the lowest centerline wake intensity for all speeds.

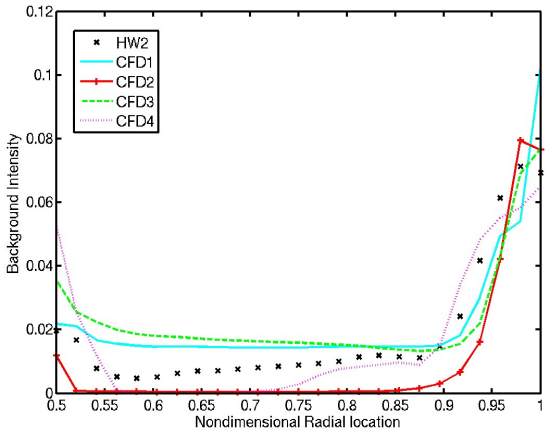

(a) Background turbulence intensity. Approach case.

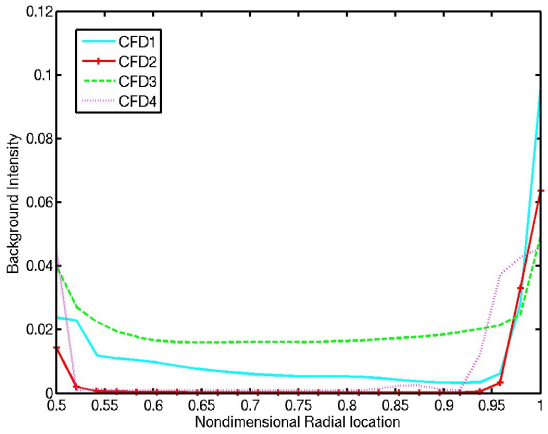

(b) Background turbulence intensity. Takeoff case.

Figure 10. Turbulence input parameters for RSI from CFD and Experiment (when available).

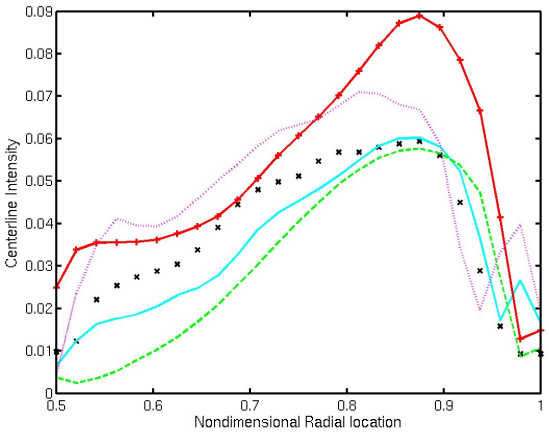

(a) Centerline turbulence intensity. Approach case

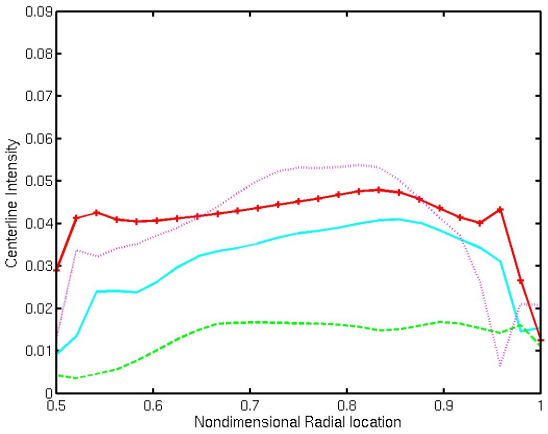

(b) Centerline turbulence intensity. Takeoff case

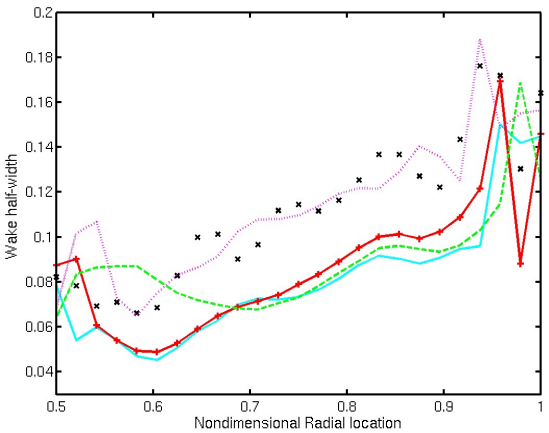

(c) FWHM. Approach case.

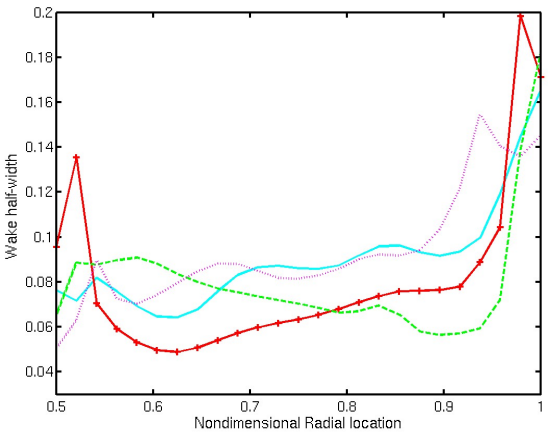

(d) FWHM. Takeoff case.

Figure 11. Turbulence input parameters for RSI from CFD and Experiment (when available).

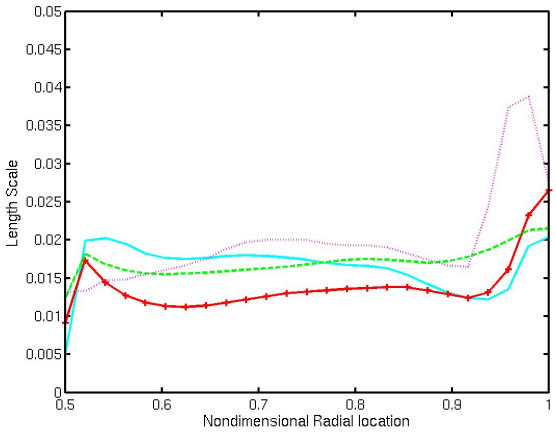

Figure 12. Length scale input from CFD for takeoff case.

V. RSI results

Figure 13 gives the exhaust PWL spectra that is computed using the inflow parameters described in the previous section. The results are shown for both the 90%/10% (leading edge) and 10%/90% (trailing edge) stagger settings. Also shown is the experimental microphone data with the rotor alone noise filtered out.[2] The length scales for the CFD cases have been set as Λ_1:Λ_2:$\Lambda_3 = \Lambda_{RANS}$:$\Lambda_{RANS}/2$:$\Lambda_{RANS}/2$.

As expected, the CFD based input with the largest length scale input (CFD4) has the highest exhaust PWLs at low frequencies and the lowest exhaust PWLs at high frequencies. The selection of leading edge stagger produces results that quantitatively match the experimentally reported broadband levels at frequencies below 10kHz however the roll-off between 10kHz and 30kHz is better matched when the trailing edge stagger is used.

To isolate the effect of the variation in length scale on the acoustic power predictions the RSI input files that represent the flow conditions from the CFD solutions have been modified. For the approach case, the length scales were modified to match the integral length scales found from the how-wire data. For the takeoff case, the length scales were modified to match the length scales from CFD2. All of the other quantities were left unchanged. Figure 14 provides the results. For the approach case, the predicted exhaust PWL spectra collapse one level. Apparent in the approach case now is the difference in background turbulence intensity levels where CFD2 and CFD4 share a lower background value as opposed to CFD1 and CFD3. For the takeoff case, there is collapse of the predictions with CFD2 and CFD4 input data which share approximately the same background levels.

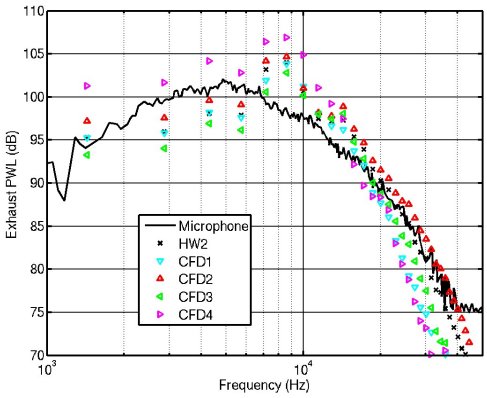

(a) Approach. 90%/10% stagger

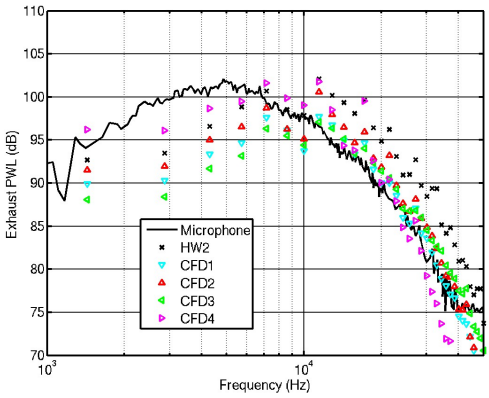

(b) Approach. 10%/90% stagger

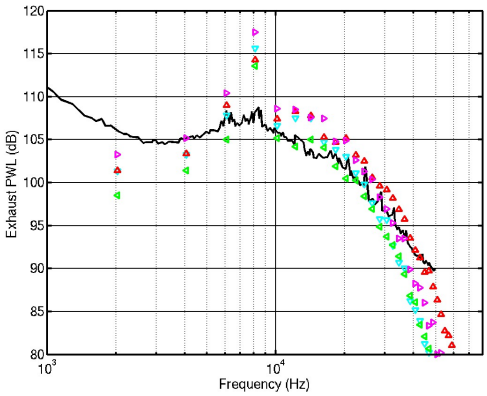

(c) Cutback. 90%/10% stagger

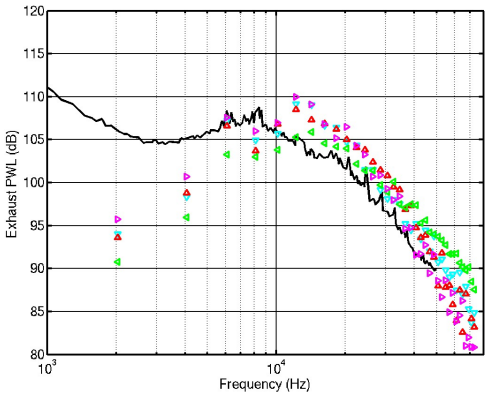

(d) Cutback. 10%/90% stagger

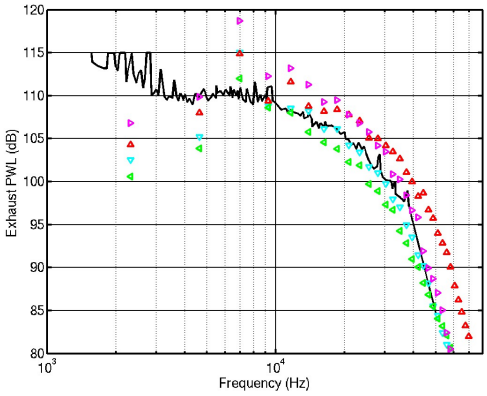

(e) Takeoff. 90%/10% stagger

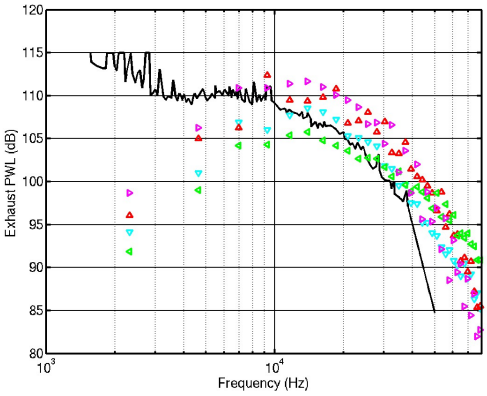

(f) Takeoff. 10%/90% stagger

Figure 13. RSI predicted Exhaust PWL from input based on CFD and HW2 (approach only).

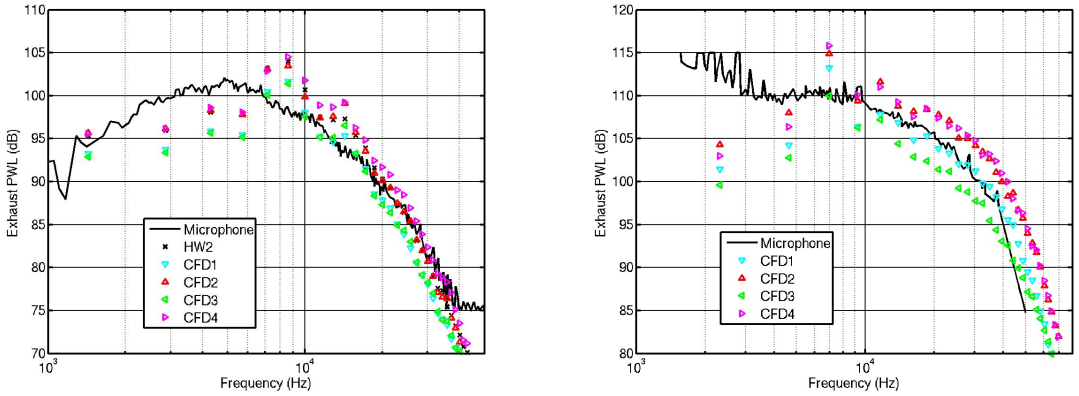

(a) HW length scale used for all cases. Approach case.

(b) CFD2 length scale used for all cases. Takeoff case.

Figure 14. Effect of length scale on Exhaust PWL Spectrum

Again these results indicate that turbulence length scale and background turbulence level in the wake are the most important inflow parameters for RSI. The prediction of length scale from RANS is slightly heuristic and the background turbulence level is specified as a RANS input which makes it a nonpredicted quantity in the end. However, there is still validity in coupling RSI to a consistent set of RANS simulations in order to predict trends. Figure 15 gives the broadband noise trend from approach to takeoff for the SDT baseline vane case. Figures 16 and 17 then show the predictions based on the hybrid method for each RANS/RSI combination. When the trailing edge stagger is selected, all of the simulated results predict that the frequency at which the broadband spectrum peaks increases slightly with wheel speed. In addition all of the simulations show a roughly 10dB increase in the broadband noise between approach and cutback and then a change of less than 5dB from cutback to takeoff. The selection of stagger that favors the leading edge stagger does not provide the correct trend although it was shown earlier that this stagger selection improved the quantitative agreement between the predictions and the experimental measurements at frequencies less than 10,000 Hz.

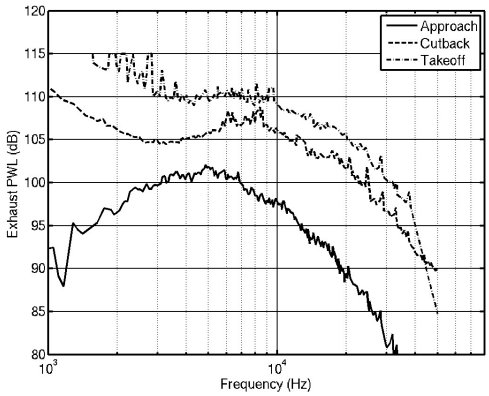

Figure 15. RSI microphone data (with rotor noise eliminated) at approach, cutback, and takeoff

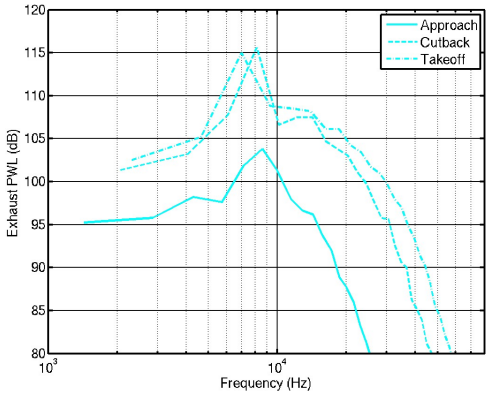

(a) CFD1. 90%-10% stagger.

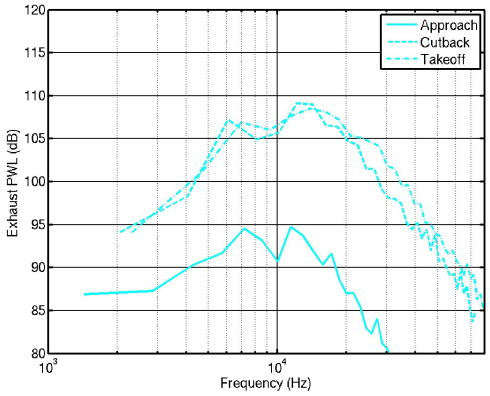

(b) CFD1. 10%-90% stagger.

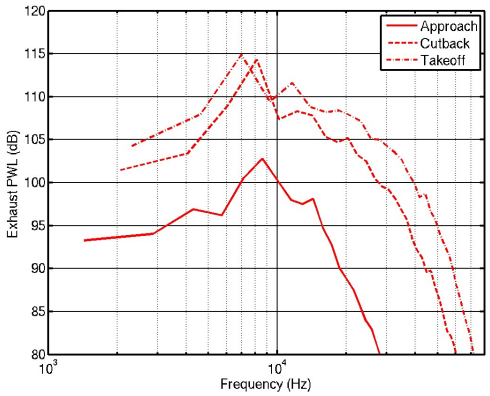

(c) CFD2. 90%-10% stagger.

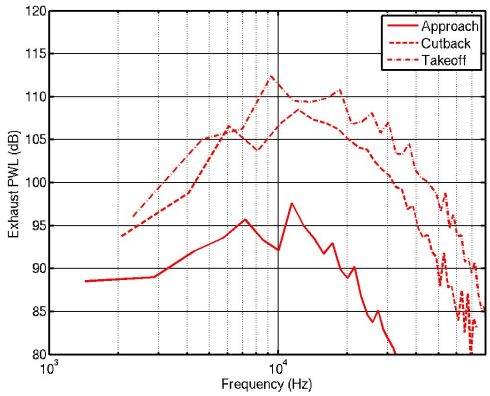

(d) CFD2. 10%-90% stagger.

Figure 16. Trends predicted using each RANS simulation set in RSI with two stagger methods.

VI. Conclusions

A fully computational method for predicting downstream broadband noise associated with rotor-FEGV interaction in a fan stage of a turbofan engine is studied. The RSI method for computing the broadband interaction noise is adopted and its sensitivity to input parameters based on RANS turbulent flow simulations is presented. The RSI method is a low order method that utilizes strip theory coupled to a two-dimensional flat-plate cascade unsteady response calculation to obtain the unsteady surface pressure spectrum on the FEGV. The acoustic pressure field at the duct exhaust is then computed using the Green's function for an annular duct. Because a flat plate model is used for the FEGVs, the selection of a stagger angle plays a role in the prediction. It is shown that changing the stagger model from one weighted heavily by the trailing edge stagger (low) to leading edge stagger (high) increases the predicted broadband noise for frequencies less than 10kHz and increases the rate of roll off above 10kHz.

For a fully computational prediction, input for the RSI calculation must come from CFD. Four RANS CFD solutions were obtained for the three rotor speeds of interest (approach, cutback, and takeoff). This paper presents comparisons of the turbulence parameters provided by the RANS simulation and hot-wire data for the approach case. The comparison highlights how CFD utilizes a scaled value of the dissipation such that the coefficient chosen for length scale calculation is 1.0. A second set of comparisons are then shown for the RSI input parameters derived from the RANS simulations. It is shown that the radial distribution of wake centerline turbulence intensity, the wake width at half maximum intensity, and the length scale all vary from the experiment and among the CFD solutions by about 50% while the background turbulent intensity input value varies by up to 100% radially with some simulations predicting almost zero background turbulence and others more than 2%.

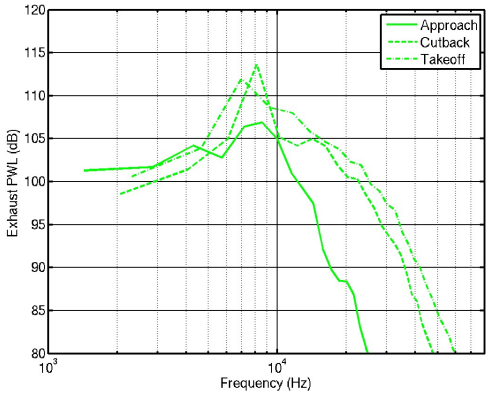

(a) CFD3. 90%-10% stagger.

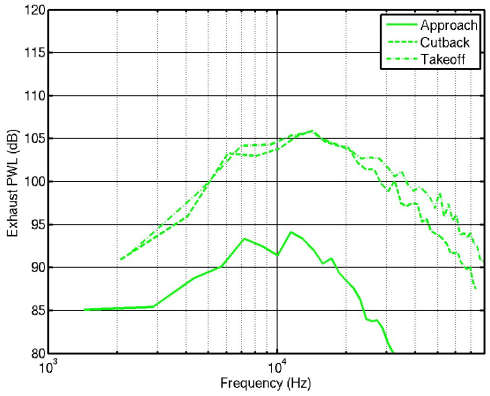

(b) CFD3. 10%-90% stagger.

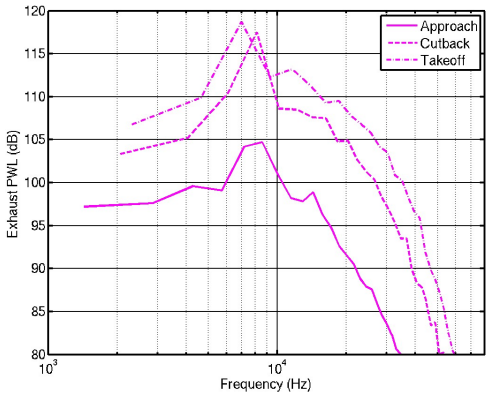

(c) CFD4. 90%-10% stagger.

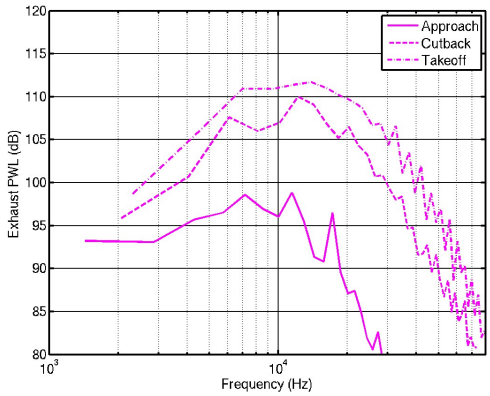

(d) CFD4. 10%-90% stagger.

Figure 17. Trends predicted using each RANS simulation set in RSI with two stagger methods.

The generic parameter study shows that when doubling and halving the turbulence related RSI input values, the background turbulence intensity modifications have the strongest effect. The second most influential input parameter is the length scale. The longitudinal length scale value plays the largest role in RSI and increases in this parameter leads to greater noise at frequencies less than 10kHz and a steeper roll off of the noise beyond 10kHz. These two parameters that most affect the prediction beyond the selection of the stagger angles; background intensity and length scale; are the most difficult to obtain with RANS. However, it is shown that across various rotor speeds, a given RANS code (run similarly) will give consistent values for the input parameters. Most importantly it is demonstrated that the trends for the downstream broadband interaction noise predicted across the rotor speeds can be captured by RSI using input based on each RANS input set when the trailing edge stagger angle is used.

Appendix A: Use of structure functions to determine dissipation

The nth order velocity increment moments, or structure functions, are defined by

$$S_n = \overline{(\delta_r \mathbf{u}')^n)} = \overline{\left((\mathbf{u}'(\mathbf{x}+\mathbf{r}) - \mathbf{u}'(\mathbf{x})) \cdot \frac{\mathbf{r}}{r}\right)^n}. \tag{22}$$

Consider the second-order longitudinal (streamwise) structure functions, S_2^s. For homogeneous, isotropic turbulence, $S_2^s(r)$, is a function only of r, the separation distance, and follows a 2/3 power law in the inertial range. Taylor's frozen turbulence hypothesis, which is valid for $u'_{rms}/U_1 << 1$, assumes that the convection of a field of turbulence can be taken to be entirely due to the mean flow, giving $r = U_1\tau$. From Taylor's hypothesis, $S_2^s(r) = S_2^s(U_1\tau)$. By definition:

$$\frac{\partial u_1}{\partial x_1} = \lim_{r\to 0} \frac{u_1(\mathbf{x}+\mathbf{r}\cdot\mathbf{i}) - u_1(\mathbf{x})}{r} = \lim_{\tau\to 0} \frac{u_1(\mathbf{x}+U_1\tau) - u_1(\mathbf{x})}{U_1\tau}, \tag{23}$$

where $\mathbf{i}$ is the unit vector in the streamwise direction. It is clear that for derivatives to be accurately evaluated the contributions on the order $O(r^2)$ must be negligibly small. This means that

$$\overline{\left(\frac{\partial u_1'}{\partial x_1}\right)^2} \approx \frac{S_2^s(r)}{r^2} \approx \frac{S_2^s(U_1\tau)}{(U_1\tau)^2} \tag{24}$$

evaluated in the analytic range of scales where $S_2^s(r) = \overline{\left(\frac{\partial u_1'}{\partial x_1}\right)^2} r^2$. Figure 18 shows the second-order structure functions in the three coordinate directions, computed at the midspan radial location at the HW2 location. For small separation times, the lateral (transverse and upwash) structure functions are approximately equal to twice the longitudinal structure functions.

The mean energy dissipation rate of locally isotropic turbulence is defined by[11,12]

$$\epsilon = 15\nu\overline{\left(\frac{\partial u_1'}{\partial x_1}\right)^2}, \tag{25}$$

and thus after considering Equation 24 the the mean energy dissipation rate can be obtained using

$$\epsilon = \lim_{\tau\to 0} 15\nu \frac{S_2^s(U_1\tau)}{U_1^2\tau^2}. \tag{26}$$

Here, ν is the kinematic viscosity. Thus, the turbulent kinetic energy dissipation rate can be directly calculated so long as the unsteady velocity measurements are taken with a short enough time-step such that for small r, $S_2(r)/r^2 \approx$ *constant*. As seen in Figure 18, a slope of 2 is approached at the sampling time of the hot-wire probes which indicates that Equation 26 is appropriate for calculating the mean energy dissipation rate. Similarly, it is readily shown that for locally isotropic turbulence ϵ can also be computed using the lateral second-order structure functions,[11,12] S_2^t and S_2^u, via

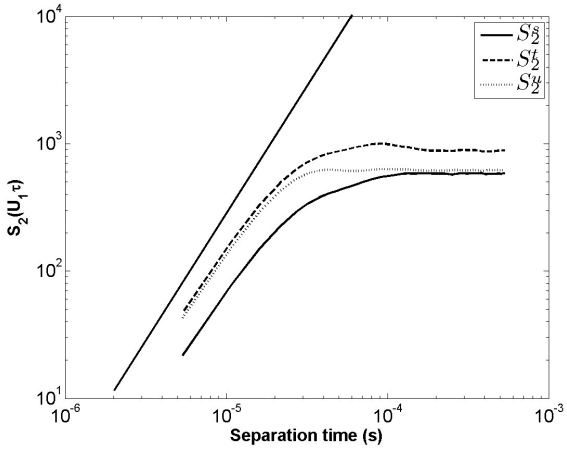

Figure 18. Midspan second-order structure functions (ft^2/s^2) at the HW2 location.

$$\epsilon = \frac{15}{2}\nu\overline{\left(\frac{\partial u_2'}{\partial x_1}\right)^2} = \lim_{\tau\to 0} \frac{15}{2}\nu \frac{S_2^t(U_1\tau)}{U_1^2\tau^2} = \lim_{\tau\to 0} \frac{15}{2}\nu \frac{S_2^u(U_1\tau)}{U_1^2\tau^2}. \tag{27}$$

Appendix B: RANS code specifications

All of the simulations have employed similar grid densities, but differ in their grid topology especially in the gap region where the wake flow exists. Table 1 provides the experimentally determined mass flows and

	Mass Flows			Pressure Ratios		
RPM	**7,808**	**11,075**	**12,657**	**7,808**	**11,075**	**12,657**
Experiment	58.30	83.91	97.18	1.159	1.360	1.509
CFD1	-	-	-	-	-	-
CFD2	58.28	83.49	97.71	1.160	1.366	1.522
CFD3	59.16	83.57	97.81	1.167	1.368	1.513
CFD4	55.82	83.80	96.96	1.160	1.349	1.503

Table 1. SDT mass flows (lb_m/s) and pressure ratios

pressure ratios,[13] as well as the mass flows and pressure ratios given by the CFD solutions for the approach, cut-back, and take-off conditions.

Some of the relevant features of the CFD simulations are described below.

- **CFD1** utilizes a version of the Wilcox $k-\omega$ turbulence model and is loosely coupled in that it simulates both the fan and the FEGV but uses a one-on-one model and handles the mismatch in blade passages via special boundary conditions. CFD1 uses O and H meshes including a square tip clearance region of 0.02 inches. The grid density between the upstream (LDV1) and downstream (LDV2) measurement stations is 95 (axial) by 64 (circumferential) by 36 (radial) points.

- **CFD2** uses a $k-\omega$ turbulence model and is also loosely coupled. CFD2 employs both C and H type grids and includes a tip clearance region of 0.04 inches. This simulation uses 86 (axial) by 89 (circumferential) by 81 (radial) grid points between the LDV1 and LDV2 axial stations.

- **CFD3** employs a $k-\epsilon$ turbulence model and utilizes the average passage method for turbomachinery flows. This simulation uses two H-grids, one in the rotor (relative) frame of reference and one in the stator (absolute) frame. The CFD3 simulation does not model the tip gap and uses 19 (axial) by 51 (circumferential) by 51 (radial) grid points between the two measurement locations for each wheel speed.

- **CFD4** is a fan-alone simulation and employs a $k-\omega$ turbulence model. This simulation uses both O and H type grids, and for the approach condition includes a tip clearance region of 0.02 inches and uses 53 (axial) by 49 (circumferential) by 113 (radial) grid points between the two LDV measurement positions. However, for the cut-back and take-off conditions, CFD4 does not model the tip gap and has a grid density of 51 (axial) by 33 by 57 points between LDV1 and LDV2.

CFD1, CFD2, and CFD3 use the "hot" rotor geometries for each wheel speed. CFD4, on the other hand, uses the approach condition's "hot" geometry for each of the three simulations. Moreover, it should be noted that the hot-wire and LDV data, to which the simulations are compared, were acquired with a 26 swept-vane (low-noise) FEGV configuration. CFD1, CFD2, and CFD3 simulate the flow field for the 54-vane baseline FEGV configuration. Additional information regarding the CFD1, CFD2, CFD3, and CFD4 turbulence models can be found in the following references:,[14–17] respectively.

Figure 19 shows the streamwise wakes at the midspan HW2 location determined from the CFD solutions and experimental data. The circumferential average has been removed for clarity. The computations capture the mean wake flow relatively well at the midspan.

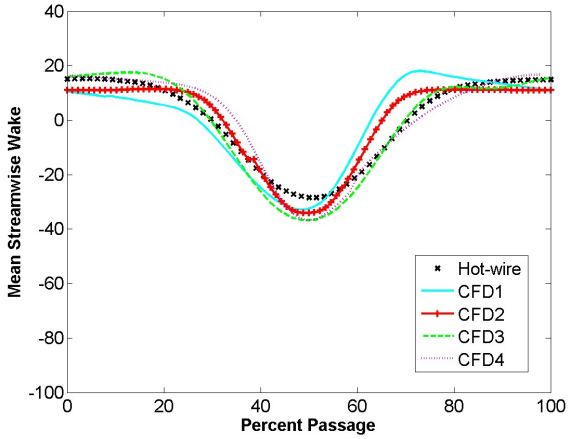

Figure 19. Midspan passagewise distribution of mean streamwise velocity (ft/s) at the HW2 location.

Appendix C: Passagewise length scale formulation

Using phenomenology and simple scaling arguments,[18] the streamwise length scale can be written in terms of the root-mean-square velocity (in the streamwise direction) and the mean dissipation rate, as

$$\Lambda_1 = C_\epsilon \frac{u_{rms}'^3}{\epsilon}. \tag{28}$$

where C_ϵ approaches a constant in the limit of large Reynolds number. Futher information concerning the coefficient C_ϵ is provided in the Appendix. As described by Donzis, Sreenivasan, and Yeung,[19] the dissipation rate of turbulent energy is independent of the fluid viscosity in the limit of large Reynolds number. This has the consequence that C_ϵ asymptotically approaches a constant in the limit of high Reynolds numbers. Doering and Foias[20] supply the following functional form

$$C_\epsilon = f(Re_\lambda) = A(1 + \sqrt{1 + (B/Re_\lambda)^2}), \tag{29}$$

where Re_λ is the Reynolds number based on the Taylor microscale, λ. In the streamwise direction the Taylor microscale is expressed by

$$\lambda_1^2 = \overline{u_1'^2} / \overline{\left(\frac{\partial u_1'}{\partial x_1}\right)^2} = \frac{15\nu\overline{u_1'^2}}{\epsilon}, \tag{30}$$

Figure 20(a), below, shows the Taylor-scale dependence of C_ϵ. These data have been fit with curves in the manner of Seoud and Vassilicos,[21] namely with C/Re_λ, where C is a constant, as well as with Equation 29. The fits of the data are $25/Re_\lambda$ (dashed line) and $0.005(1 + \sqrt{1 + (4500/Re_\lambda)^2})$ (solid line). Donzis, Sreenivasan, and Yeung note that while the asymptotic dependence of C_ϵ shown in Figure 20(a) is universal for all types turbulent flows away from solid walls, it must be emphasized that "the coefficients A and B are not universal, even if one fixes the operational definitions of Λ_1 and u_1'. They depend on the type of flow, and, for a given flow, on detailed initial conditions.[19]" Subsequently, the passage distribution of the streamwise integral length scales can be computed with equations 29 and 30 and the value of C_ϵ from the curve fit.

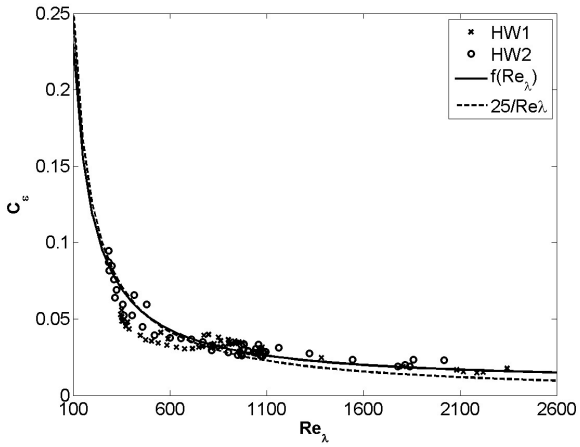

Figure 20. C_ϵ versus Re_λ

Acknowledgments

The authors would like to thank Drs. A, Sharma, B. Morin, and E. Envia for providing CFD simulation results for the SDT cases. The authors would also like to recognize the following people (from NASA Glenn unless otherwise noted): CFD code development: Daniel L. Tweedt, (AP Solution Inc.), Timothy A. Beach, Amir A. Shabbir, Mark A. Celestina, Scott A. Thorp, Richard A. Mulac, and John J. Adamczyk (retired); SDT sideline acoustics data: Richard P. Woodward; and SDT hotwire/LDV wake data: Gary G. Podboy. Additional recognition is given to Dr. Envia for his continued development and sharing the RSI code. Professor Victor Yakhot from the ME Dept. at BU is acknowledged for his contributions to the analysis of the experimental data. Finally the authors acknowledge the financial support of the Aeroacoustics Research Consortium through the Ohio Aerospace Institute grant R-700-400301-40125 and the collaboration of the AARC members.

References

[1] Hanson, D. B. and Horan, K. P., "Turbulence/Cascade Interaction – Spectra of Inflow, Cascade Response, and Noise," *AIAA Paper No. 98-2319*, 1998, 4th AIAA/CEAS Aeroacoustics Conference.

[2] Nallasamy, M. and Envia, E., "Computation of rotor wake turbulence noise," *Journal of Sound and Vibration*, Vol. 282, 2005, pp. 649–678.

[3] Envia, E., Tweedt, D., Woodward, R. P., Elliot, D. M., Fite, E. B., Hughes, C. E., Podboy, G. G., and Sutliff, D. L., "Assessment of Current Fan Noise Prediction Capability," *AIAA Paper No.2008-2991*, 2008, 14th AIAA/CEAS Aeroacoustics Conference.

[4] Atassi, H. M. and Logue, M. M., "Effect of Turbulence Structure on Broadband Fan Noise," *AIAA Paper No. 2008-2842*, 2008, 14th AIAA/CEAS Aeroacoustics Conference.

[5] Ventres, C., Theobald, M. A., and Mark, W. D., "Turbofan Noise Generation Volume 1: Analysis," Tech. Rep. CR-167952, NASA, July 1982.

[6] Podboy, G. G., Krupar, M. J., Helland, S. M., and Hughes, C., "Steady and Unsteady Flow Field Measurements Within a NASA 22-Inch Fan Model," Tech. Rep. TM-2003-212329, NASA, 2003.

[7] Camp, T. and Shin, H.-W., "Turbulence intensity and length scale measurements in multistage compressors," *Journal of Turbomachinery*, Vol. 117, January 1995, pp. 38–46.

[8] Axelsson, L.-U. and George, W., "Spectral Analysis of the flow in an intermediate turbine duct," *ASME*, Vol. 6, 2008, pp. 1419–1426, ASME Turbo Expo 2008: Power for Land, Sea, and Air (GT2008).

[9] Maunus, J., *Effect of Rotor Wake Structure on Fan Interaction Noise*, MS Thesis, Boston University, Boston, MA, January 2011.

[10] Maunus, J., Grace, S. M., Sondak, D. L., and Yakhot, V., "Investigation of Calculated Turbulence Parameters for use in Hybrid Broadband Fan Noise Calcula- tions," *GT2011-45906*, 2011, ASME Turbo Expo 2011: Power for Land, Sea, and Air (GT2011).

[11] Kolmogorov, A., "Dissipation of Energy in the Locally Isotropic Turbulence," *Proceedings: Mathematical and Physical Sciences*, Vol. 434-1890, 1991, pp. 15–17.

[12] Monin, A. S. and Yaglom, A., *Statistical Fluid Mechanics: Mechanics of Turbulence Volume II*, MIT Press, Cambridge, MA, 1971.

[13] Hughes, C. E., Jeracki, R. J., Woodward, R. P., and Miller, C. J., "Fan Noise Source Diagnostic Test - Rotor Alone Aerodynamic Performance Results," Tech. Rep. TM-2005-211681, NASA, 2005.

[14] Holmes, D. and Lorence, C., "Three Dimensional Linearized Navier-Stokes Calculations For Flutter and Forced Response," *Proceedings of the Eighth International Symposium on Unsteady Aerodynamics and Aeroelasticity of Turbomachines*, 1997, pp. 211–224.

[15] Chima, R., "A $k - \omega$ Turbulence Model for Quasi-Three-Dimensional Turbomachinery Flows," Tech. Rep. 107051, NASA, September 1995.

[16] Shih, T.-H., Liou, W., Shabbir, A., Yang, Z., and Zhu, J., "A New $k - \epsilon$ Eddy Viscosity Model for High Reynolds Number Turbulent Flows - Model Development and Validation," Tech. Rep. 106721, NASA, August 1994.

[17] Menter, F., "Improved Two-Equation $k - \omega$ Turbulence Modesl for Aerodynamic Flows," Tech. Rep. 103975, NASA, October 1992.

[18] Frisch, U., *Turbulence: The Legacy of A.N. Kolmogorov*, Cambridge University Press, Cambridge, UK, 1995.

[19] Donzis, D. A., Sreenivasan, K. R., and Yeung, P. K., "Scalar dissipation rate and dissipative anomaly in isotropic turbulence," *Journal of Fluid Mechanics*, Vol. 532, 2005, pp. 199–216.

[20] Doering, C. R. and Foias, C., "Energy dissipation in body-forced turbulence," *Journal of Fluid Mechanics*, Vol. 467, 2002, pp. 289–306.

[21] Seoud, R. and Vassilicos, J., "Dissipation and decay of fractal-generated turbulence," *Physics of Fluids*, Vol. 19, 2007, pp. 105108–105108–11.